

Xe gas bubble re-resolution in U-10Mo nuclear fuel

ATM Jahid Hasan¹, Linu Malakkal², Mathew Swisher², and
Benjamin Beeler^{1,2,*}

¹North Carolina State University

²Idaho National Laboratory

March 16, 2026

Abstract

The U.S. High-Performance Research Reactor program aims to convert high-power research reactors from highly enriched uranium to low-enriched uranium using a monolithic U-10Mo fuel design. A critical aspect of U-10Mo fuel performance is fission gas bubble behavior. These bubbles grow by trapping gas atoms (particularly Xe) but can disintegrate via irradiation-induced “re-resolution”. The interplay between the trapping and re-resolution rates governs bubble evolution, impacting fuel performance and safety. In this study, binary collision approximation (BCA) and molecular dynamics (MD) simulations were performed to quantify the Xe gas bubble re-resolution rate in U-10Mo fuel. First, the energy loss of fission fragments (FFs) through electronic and nuclear stopping was evaluated. The effect of electronic stopping on re-resolution was then analyzed using MD simulations coupled with the two-temperature model. Results indicate that thermal spikes generated by electronic stopping do not contribute to gas bubble re-resolution in U-10Mo. To quantify re-resolution due to nuclear stopping, BCA simulations of FFs in U-10Mo were performed to obtain the average FF incidence probability, energy, and angle as a function of distance from the FF origin. Subsequent simulations assessed FF–bubble interactions in U-10Mo for different FF energies and bubble radii. From these analyses, an overall re-resolution rate b was calculated at equilibrium bubble pressure per unit fission rate density, yielding values ranging from 4.4×10^{-26} m³/fission for the largest bubbles to 8.8×10^{-25} m³/fission for the smallest. The effect of bubble pressure on the re-resolution rate was also evaluated, revealing an inverse relationship between the two.

*Corresponding author. Email: bwbeeler@ncsu.edu.

1 Introduction

A U-10Mo alloy-based monolithic fuel design was selected as the fuel type for converting U.S. High-Performance Research Reactors (HPRRs) [1] from highly enriched uranium (HEU) fuel to low-enriched (LEU) fuel. To reliably predict the fuel’s behavior under irradiation, mesoscale and engineering-level fuel performance models require knowledge of the fundamental mechanistic behavior of fission products within the fuel to describe key phenomena, such as swelling [2, 3]. Specifically, understanding the progression of Xe gas bubbles in the fuel is crucial for optimizing reactor performance and safety. These gas bubbles act as a sink for diffusing Xe atoms in the fuel, whose subsequent entrapment leads to progressive bubble growth. Conversely, under irradiation, the Xe atoms in the gas bubbles are reintroduced into the fuel matrix through collision cascades and thermal spikes produced by fission fragments (FFs)—a process referred to as “re-resolution”. The relative rates of Xe trapping and re-resolution dictate the size and density of the gas bubbles [4, 5, 6], thereby influencing bubble evolution and the overall swelling behavior of the fuel.

There are two widely accepted mechanisms of fission gas bubble re-resolution: homogeneous re-resolution and heterogeneous re-resolution [5]. In the homogeneous model proposed by Nelson [7], individual atoms are ejected from gas bubbles via collisions with energetic FFs or recoil atoms traversing the bubbles. These atomic collision cascades are primarily governed by the nuclear stopping power of the material. In contrast, in the heterogeneous model proposed by Turnbull [8], a portion of the gas bubbles is dissolved by FFs passing in their vicinity. The driving mechanism is the local heating of the material containing the gas bubbles, through the electronic stopping of the FFs [9]. Irrespective of the mechanism, the re-resolution rate b is defined as the fraction of gas atoms returned to the solid solution from bubbles per unit time, or equivalently, the probability per unit time of a single gas atom being ejected from a bubble back into the lattice [5, 9]. Since both mechanisms occur on very short timescales, experimentally determining the re-resolution rates required for fission gas release models becomes challenging. As a result, atomic-scale simulations are essential to elucidate the underlying mechanisms and provide a quantitative description of the re-resolution process in U-10Mo.

In the literature up to this point, atomistic simulations have been widely used to evaluate the re-resolution rate in various nuclear materials. For instance, in 2008, Parfitt et al. [6] simulated primary knock-on atoms (PKAs) in uranium dioxide (UO₂) using molecular dynamics (MD) to assess the re-resolution of helium gas bubbles. In 2009, Schwen et al. [10] investigated the homogeneous re-resolution of Xe gas bubbles in UO₂, using binary collision approximation (BCA) and MD. The following year, Huang et al. [11] examined the impact of thermal spikes on Xe re-resolution in UO₂ using MD coupled with the two-temperature model (TTM). In 2012, Govers et al. [12] performed MD simulations to study how PKA and thermal spikes interact with Xe gas bubbles in UO₂ and proposed a mathematical model to describe the observed re-resolution. The most comprehensive work on Xe gas bubble re-resolution in UO₂ was conducted in 2018 by Setyawan et al. [9]. They reconciled the inconsistencies found in the conclusions of previous works on Xe bubble re-resolution in UO₂ and evaluated the re-resolution rate as a function of bubble radius with the help of extensive MD simulations. Their results suggest that heterogeneous re-resolution of gas bubbles is the dominant method of re-resolution in UO₂. In addition to UO₂, the re-resolution rate of fission gas bubbles has also

been evaluated in other nuclear materials. Matthews et al. [13] evaluated re-resolution in uranium carbide (UC) in 2015, while Mao et al. [14] studied re-resolution in uranium-zirconium (U-Zr) alloys in 2025, both using BCA simulations. Unlike with UO_2 , thermal spikes are not expected to occur in UC and U-Zr systems, due to their higher electronic conductivities and thermal diffusivities [15, 13, 14]. Thus, only homogeneous re-resolution has been studied in UC and U-Zr. In summary, both BCA and MD simulations have been utilized to determine re-resolution rates in nuclear fuels.

MD simulations of homogeneous re-resolution typically involve assigning a high kinetic energy to a regular lattice atom in order to emulate a PKA. The PKA then interacts ballistically with other atoms, initiating a collision cascade near the gas bubble and inducing localized atomic disorder [6, 12]. One alternative MD approach focuses on simulating a subcascade by imparting energy directly to a random gas atom within the bubble. This method reduces computational costs by avoiding unnecessary cascade events that may not significantly influence the re-resolution process. However, to implement this approach accurately, BCA simulations are required in order to first obtain an energy spectrum of gas atom PKAs [10]. One challenge in modeling homogeneous re-resolution with MD is the channeling of PKAs or their recoils over long distances, without undergoing significant collisions [16]. This phenomenon can make it computationally demanding to gather statistics on interactions between PKAs and gas bubble atoms, particularly when PKA directions are assigned randomly. A potential solution is to direct the PKAs along high-index lattice directions [17], thus increasing the collision probability. Additionally, collision cascades often produce heat spikes due to nuclear stopping, which induce defect formation and facilitate damage-assisted re-resolution. Ballistically re-resolved atoms can then be differentiated by employing a threshold atomic speed that is highly improbable to occur in normal thermal equilibrium of the bubble at the lattice temperature prior to the cascade initiation [6].

For heterogeneous re-resolution, MD simulations of thermal spikes are commonly employed. FFs lose a significant portion of their energy via electronic stopping, with the deposited energy initially raising the temperature of the electronic subsystem. The energy is subsequently transferred to the lattice as thermal energy via electron-phonon coupling, leading to a rapid rise of lattice temperature within a cylindrical zone of typically a few nanometers in radius. This localized heating, known as a thermal spike [18, 19, 20], can induce re-resolution if the spike intersects a gas bubble. Although MD simulations cannot model electronic interactions directly, the thermal spike process can be approximated by either instantaneously increasing the temperature of atoms in a cylindrical region [12, 9] or by coupling MD with the TTM [21, 11].

Accurate prediction of fission gas behavior under various operational and transient conditions is critical for the qualification of U-10Mo fuel. To this end, the Dispersion Analysis Research Tool (DART), a mesoscale code developed by Argonne National Laboratory [4], has been equipped with the ability to calculate fission gas swelling in U-10Mo under a range of operating conditions. DART employs a re-resolution model that includes a piecewise function to account for both intragranular (typically with radii ≤ 2.5 nm) and intergranular gas bubbles (typically with radii > 2.5 nm) [22]. However, the parameters of this model are calibrated by fitting the computed swelling values to experimental data, providing only a rough estimation of the re-resolution rate. A physics-based model of the re-resolution rate would enhance the predictive capability of the higher-length-scale swelling models. In this study,

we utilized BCA and MD simulations to investigate the re-resolution of Xe gas bubbles in U-10Mo fuel, addressing both the homogeneous and heterogeneous re-resolution mechanisms. This work intends to provide a mechanistic understanding of the re-resolution process in U-10Mo, enabling more rigorous modeling of fission gas behavior and swelling in the fuel under various reactor conditions.

2 Computational methods

In this section, we outline general computational methods used in this study. For better readability, specific simulation parameters and implementation details are discussed along with the results.

2.1 Binary collision approximation

RustBCA, an open-source software for simulating ion-material interactions [23], was used for all BCA simulations in this work. RustBCA supports a variety of ion-material interactions, including sputtering, implantation, and reflection. Out of the box, RustBCA supports infinite homogeneous 0D targets, finite-depth layered inhomogeneous 1D targets, inhomogeneous 2D targets through a triangular mesh, and homogeneous 3D triangular mesh geometry. However, it does not support inhomogeneous 3D geometry, which is necessary to emulate gas bubbles embedded in solids. For this reason, we implemented a custom 3D geometry in RustBCA termed SPHEREINCUBOID. This configuration enables the user to specify a spherical material inside a distinct cuboid material. The source code for this implementation is available at <https://github.com/ATM-Jahid/RustBCA>. Like most BCA codes, RustBCA assumes an amorphous, static material, neglecting crystal structures and accumulation of irradiation damage. It also cannot take into account temperature effects.

Electronic stopping in the BCA simulations performed in this work was described by the Biersack-Varelas interpolation [24], and the nuclear interactions were described by the universal Kr-C potential [25, 26]. An exponentially distributed mean-free-path model was used for gaseous regions and a constant mean-free-path model for solid regions. A threshold number density of $1.5 \times 10^{28} \text{ m}^{-3}$ was used to distinguish between the gaseous and solid regions.

2.2 Molecular dynamics

The LAMMPS software package [27] was utilized to perform MD simulations, using a U-Mo-Xe angular-dependent potential [28, 29, 30]. This angular-dependent potential can accurately describe the body-centered cubic (bcc) phase of γ U-Mo alloys, effectively reproducing their stable structure, elastic modulus, room temperature density, and melting point. To emulate the electronic stopping of the FFs, all MD simulations were coupled with the TTM using the `ttm/mod` command in LAMMPS [31, 32]. This approach treats the electronic subsystem as a continuum while describing the ionic subsystem through standard MD. Energy transfer within the electronic subsystem is governed by the heat diffusion equation, which includes

source terms to model the heat transfer between the electronic and ionic subsystems:

$$C_e(T_e)\rho_e\frac{\partial T_e}{\partial t} = \nabla(\kappa_e\nabla T_e) + g_p(T_e - T_a) \quad (1)$$

where C_e represents the electronic specific heat as a function of electronic temperature T_e , ρ_e is the electronic density, κ_e is the electronic thermal conductivity, g_p is the coupling constant for electron-ion interactions, and T_a is the ionic temperature [21, 33]. The electronic specific heat was expressed as $C_e = \gamma T_e$, where $\gamma = 4 \times 10^{-9}$ eV/(K²e). The electronic density was set to $\rho_e = 625$ e/nm³, and the thermal conductivity was calculated using $\kappa_e = D_e\rho_e C_e$, where $D_e = 100$ nm²/ps is the thermal diffusion coefficient [34, 35]. Although these TTM parameter values have only been used for pure U or U-5at.%Mo, it is assumed that reasonable accuracy can be obtained with these values for the U-10Mo system as well.

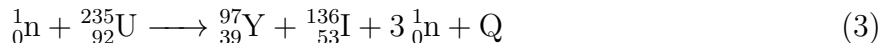
Electronic pressure effects were included in the model to account for the blast force acting on ions due to the electronic pressure gradient [36, 31]. Thus, the total force acting on an ion is:

$$\vec{F}_i = -\frac{\partial U}{\partial \vec{r}_i} + \vec{F}_{langevin} - \nabla P_e/n_{ion} \quad (2)$$

where $\vec{F}_{langevin}$ is the force from the Langevin thermostat simulating electron-phonon coupling, U is the potential energy of the system, $\nabla P_e/n_{ion}$ is the electron blast force, and n_{ion} is the ion concentration. The electronic pressure was modeled as $P_e = 0.5\rho_e C_e T_e$ [31, 32, 35].

3 Energy loss of fission fragments in U-10Mo

To understand and quantify re-solution in U-10Mo, FF behavior must first be investigated. Fission of ²³⁵₉₂U produces a wide range of isotopes. To keep computational complexity manageable, two isotopes, ⁹⁷₃₉Y and ¹³⁶₅₃I, were selected as representative light and heavy FFs, respectively. These isotopes are produced in the fuel via the following nuclear reaction:



While ⁹⁷₃₉Y has an initial kinetic energy of approximately 101.3 MeV, ¹³⁶₅₃I starts with roughly 74.6 MeV. These two isotopes were chosen because they correspond to the two peaks commonly observed in fission product yield distributions, and they each have a yield of about 0.12 [9, 37].

To evaluate the energy loss of these FFs in U-10Mo, BCA simulations were conducted using RustBCA's 0D geometry option. In these simulations, U-10Mo was modeled as an infinite medium extending from 0 to ∞ in the x direction, and from $-\infty$ to ∞ in the y and z directions. The FFs were injected at the origin with an initial velocity oriented along the x axis. For each FF, 2,000 independent ion-material simulations were performed. From these simulations, FF positions and velocities from each binary collision were recorded, then processed and binned to obtain electronic and nuclear stopping power profiles, as illustrated in Figure 1. At the beginning of the FF trajectories, the electronic stopping power is slightly less than 20 keV/nm for both FFs and decreases almost linearly with distance. In contrast,

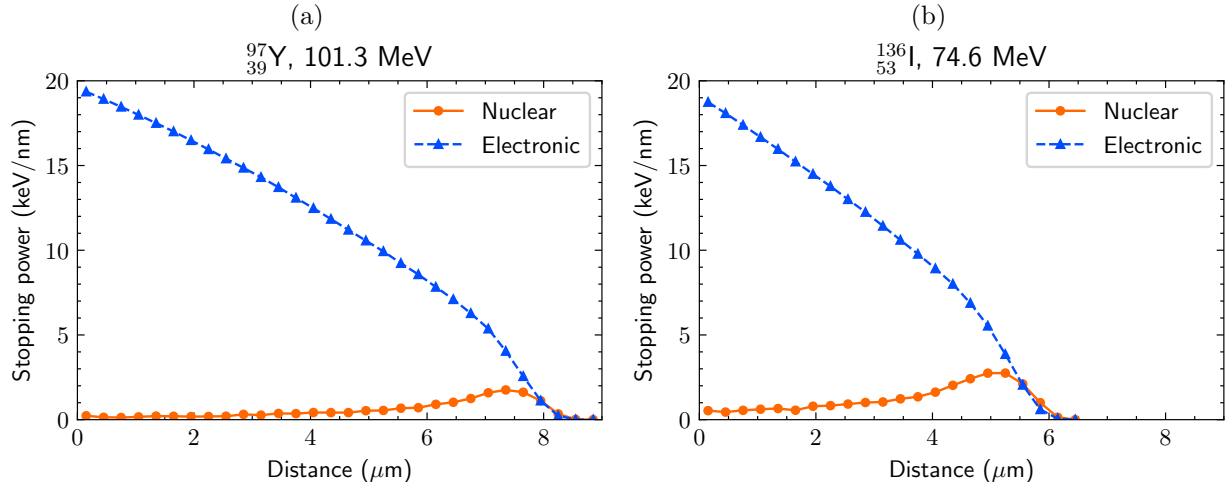


Figure 1: **Nuclear and electronic stopping powers of FFs.** Nuclear and electronic stopping powers of (a) light FF $^{97}_{39}\text{Y}$ with an initial energy of 101.3 MeV, and (b) heavy FF $^{136}_{53}\text{I}$ with an initial energy of 74.6 MeV as a function of distance in U-10Mo. Data were obtained from 2,000 independent BCA simulations for each FF using RustBCA.

the nuclear stopping power remains low for the majority of the FF trajectory, peaking only at the very end of the path as the FF reaches energies where nuclear collisions become more probable. The nuclear energy loss for $^{97}_{39}\text{Y}$ accounts for approximately 5% of its total initial energy, whereas for $^{136}_{53}\text{I}$, the nuclear energy loss is around 10%.

Using insights derived from the stopping power profiles, two complementary methods were employed to investigate gas bubble re-resolution in U-10Mo. To analyze the effect of electronic stopping, the TTM was utilized to simulate the energy transfer between the electronic subsystem and the ionic subsystem (discussed further in Section 4). To capture the effect of nuclear stopping on re-resolution, the interactions among FFs, U-10Mo, and Xe gas bubbles were simulated using the newly implemented SPHEREINCUBOID geometry in RustBCA, as detailed in Section 5.

4 Re-resolution due to electronic stopping

To simulate thermal spikes, a simulation cell with dimensions $120\alpha_0 \times 120\alpha_0 \times 50\alpha_0$ ($\alpha_0 = 0.343$ nm is the lattice parameter of U-10Mo at 400 K [38]) was created with periodic boundary conditions in all directions. A random distribution of U and Mo atoms in a bcc lattice was first generated to achieve a Mo concentration of 22 at.%. Using this configuration, a spherical gas bubble with a radius of 2 nm was created by removing U and Mo atoms and depositing Xe atoms inside the void. The Xe gas atoms were introduced at a Xe/vacancy ratio of 0.2, resulting in approximately 330 Xe atoms within the bubble. The system was equilibrated at 400 K and 0 bar by using an NPT ensemble for 10 ps, with a timestep size of 1 fs. The Nosé-Hoover thermostat and barostat regulated the temperature and pressure during equilibration. The bubble size and Xe/vacancy ratio at the prescribed temperature and pressure follow the results from the equation of state of Beeler et al. [39].

To solve heat transfer related to the electronic subsystem, electronic cells with dimensions $2\alpha_0 \times 2\alpha_0 \times 50\alpha_0$ were defined across the whole simulation cell, with periodic boundary conditions applied in all directions. A thermal spike was introduced by initializing the electronic temperature profile in these cells according to:

$$T_e = T_{init} + T_{spike} \exp(-r/R) \quad (4)$$

where r is the radial distance from the thermal spike axis, $R = 10\alpha_0$, and $T_{init} = 400$ K. The thermal spike axis was aligned with the shortest dimension of the supercell. The values of T_{spike} were chosen according to the desired electronic stopping power. The simulations were then performed using an NVE ensemble with a canonical sampling thermostat [40] applied at the edges of the simulation box to serve as a heat sink. Only those edges that did not intersect the thermal spike axis were included in the heat sink region. A variable timestep size was implemented such that the maximum displacement of any atom between two successive timesteps was less than or equal to 0.001 nm. 100,000 timesteps were performed for each simulation, yielding 80–90 ps of total simulation time.

Simulations were performed with three values of T_{spike} (28,000 K, 31,500 K, and 34,500 K), corresponding to electronic stopping powers ranging from 20 keV/nm to 30 keV/nm. No re-resolution events were observed in any of these simulations. Figure 2 presents a few snapshots of a 30 keV/nm thermal spike simulation as visualized in OVITO [41]. The local ionic subsystem temperature rises rapidly for about 1.5 ps following the initiation of the thermal spike, reaching its peak before beginning to cool. After 30 ps, only a few defects are visible within the system. The local temperature gradually returns to the initial equilibrium temperature over approximately 60 ps.

Kolotova et al. reported threshold electronic stopping powers for defect formation and melting in U-5at.%Mo at various temperatures [35]. At 400 K, the threshold stopping powers for defect formation and melting were found to be approximately 22 keV/nm and 26 keV/nm, respectively. Given that 1) no gas bubble re-resolution was observed in the MD simulations of 30 keV/nm thermal spikes, 2) peak stopping power of FFs in U-10Mo is approximately 20 keV/nm (Figure 1), and 3) threshold stopping power for defect formation exceeds 20 keV/nm, it is highly unlikely that gas bubble re-resolution can occur in U-10Mo through the heterogeneous mechanism. This behavior is expected since U-10Mo is a metallic system and displays a relatively high thermal conductivity, but it has been explicitly confirmed here for the first time.

5 Re-resolution due to nuclear stopping

5.1 Model for re-resolution calculation

The re-resolution rate can be defined as the probability of a Xe atom escaping a gas bubble and entering the surrounding fuel matrix, per unit time. To capture the overall re-resolution behavior in the material, the contributions from all the FFs, originating at various distances from the bubble and oriented toward random directions, must be integrated over the entire volume of interest. Consider a 3D coordinate system in which the gas bubble is located at the origin. To simplify the integration, FF points of origin can be rotated around the

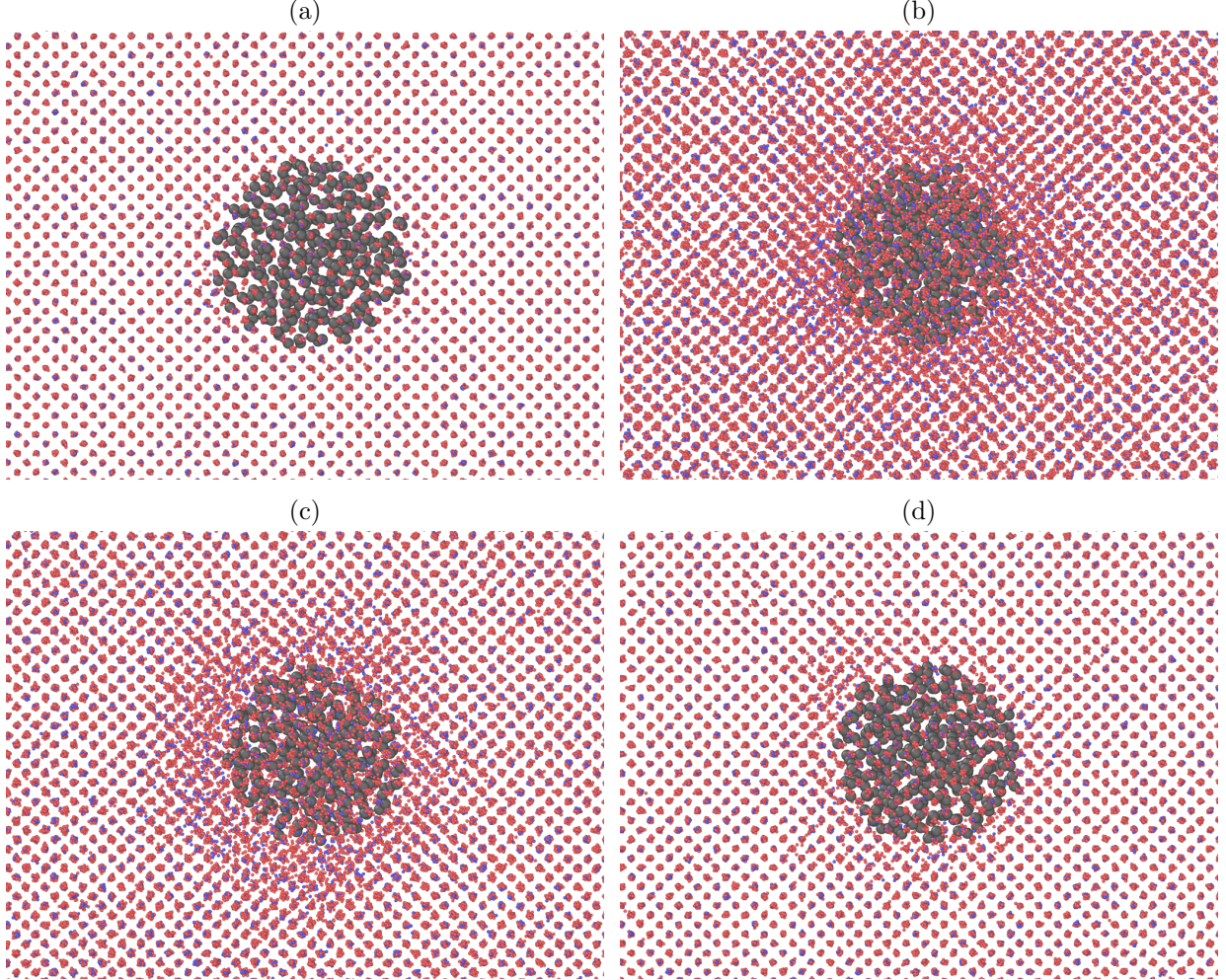


Figure 2: **Temporal evolution of a thermal spike simulation in U-10Mo.** Snapshots of a 30 keV/nm thermal spike simulation at (a) 0 ps, (b) 2.4 ps, (c) 10.1 ps, and (d) 29.1 ps. Xe gas atoms are represented in black, U in red, and Mo in blue. The local ionic temperature rises rapidly for 1.5 ps before beginning to cool. No Xe atom was observed to escape the gas bubble. The images were rendered using OVITO.

coordinate system origin such that their initial velocities align in the same direction. Since FF generation in the material is uniform and isotropic, this rotational transformation results in a uniform distribution of unidirectional FFs, as shown in Figure 3a. The axial coordinate x is then defined as parallel to the FF velocities (which are now directed toward $-x$), whereas the radial coordinate $w := \sqrt{y^2 + z^2}$ is defined as perpendicular to the velocities (Figure 3b). If the fission rate is denoted as \dot{F} , the number of fission events per second in an infinitesimal volume $dV = 2\pi w dw dx$ would be $\dot{F}dV$. Also, we assume that when a FF isotope k originating at (x, w) interacts with a Xe gas bubble at the origin, it re-solves a fraction, $\xi_k \equiv \xi_k(x, w)$, of the Xe atoms. All the k isotopes from fission events in dV thus contribute $\xi_k(x, w)\dot{F}dV$ to the total re-resolution of the bubble. The re-resolution rate b can

then be expressed as:

$$b = \sum_{k=Y,I} \int_V \xi_k(x, w) \dot{F} dV \quad (5)$$

$$= \dot{F} \sum_{k=Y,I} \int_V \xi_k(x, w) dV = \dot{F} \left(\int_V \xi_Y(x, w) dV + \int_V \xi_I(x, w) dV \right) \quad (6)$$

$$= \dot{F} \sum_{k=Y,I} \int_{x=0}^{\infty} \int_{w=0}^{\infty} \xi_k(x, w) 2\pi w dw dx \quad (7)$$

where it is assumed that all fission events produce $^{97}_{39}\text{Y}$ and $^{136}_{53}\text{I}$, as per Equation 3.

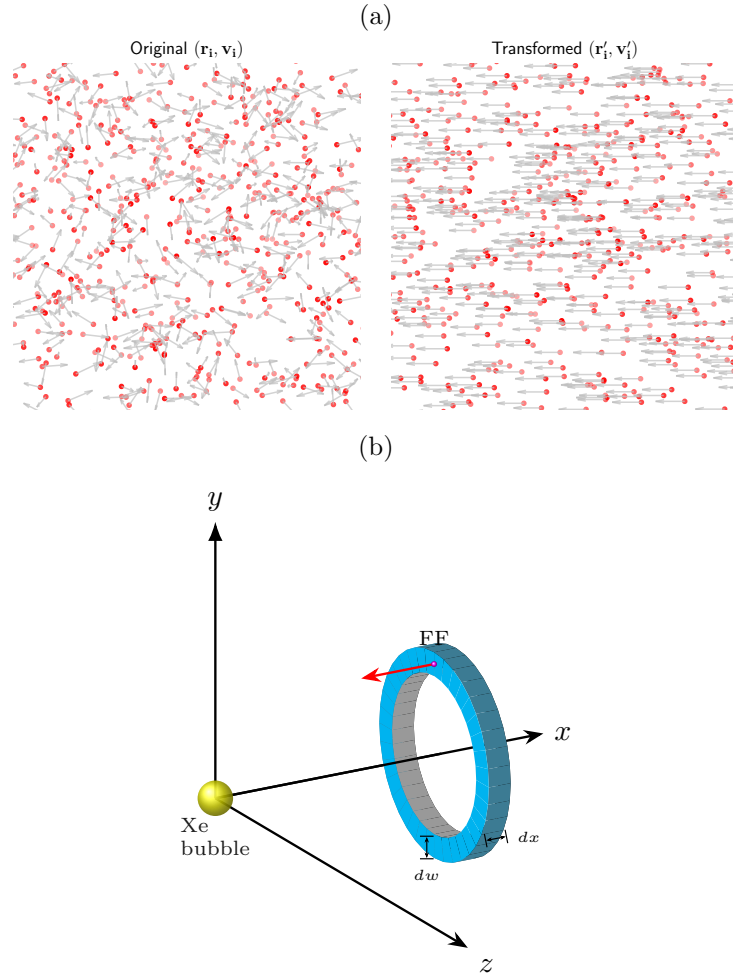


Figure 3: **Coordinate system for the calculation of the re-solution rate.** **a** Rotation of fission event positions and velocities around the origin such that all velocities point to the $-x$ direction. Red dots represent positions and gray arrows represent velocities. **b** A coordinate system in which a Xe gas bubble is at the origin and FFs are all pointing toward the $-x$ direction. The radial coordinate $w = \sqrt{y^2 + z^2}$ represents the perpendicular distance between the initial FF trajectory and the bubble center.

5.2 Reference fission fragment simulations

The most straightforward method to calculate $\xi_k(x, w)$ involves simulating a FF and a Xe gas bubble for a specific (x, w) value. However, performing these simulations for all required (x, w) values is computationally expensive and often yields statistically unreliable results. As the distance between the origin of a given FF and a Xe gas bubble increases, the probability of interaction between them decreases significantly. The interaction probability is also influenced by the size of the gas bubble: smaller bubbles exhibit a lower probability of interaction. Therefore, for certain bubble sizes and (x, w) values, even conducting hundreds of thousands of BCA simulations may result in only a few interactions, making most of these simulations an inefficient use of computational resources.

An alternative to the brute-force approach involves analyzing the behavior of FFs in the fuel matrix without the presence of any gas bubbles first. If the probability of a FF passing through a specific point in the fuel with a given energy is known, assessing re-solution behavior from local FF–bubble interactions at that exact point then becomes straightforward. Thus, FF simulations in U-10Mo were performed to obtain three key properties for each (x, w) coordinate: the probability of a FF passing through a unit surface area centered at (x, w) , its average incidence energy, and its average incidence angle relative to the x axis. In these reference simulations, the FF started from the origin and was directed toward the x axis within a U-10Mo matrix, as displayed in Figure 4a. It is important to note that this setup is inverted from the configuration shown in Figure 3b, where the Xe gas bubble is positioned at the origin.



Figure 4: **FF trajectory discretization scheme.** **a** Trajectories of 100 simulated $^{97}_{39}\text{Y}$ ions in U-10Mo, starting from the origin and directed along the x axis. **b** Schematic of the annular surface discretization scheme used to collect data across the volume. The discretization allows for the extraction of three key properties at each (x, w) coordinate: the probability of a FF passing through a unit surface area centered at (x, w) , its average incidence energy, and its average incidence angle relative to the x axis. The simulation volume is discretized using a two-dimensional grid with uniform spatial intervals of $\Delta x = \Delta w = 50$ nm.

To collect data from the simulations, an annular surface discretization scheme, as illustrated in Figure 4b, was used. The discretized surface elements were associated with specific (x, w) values, with the spacing between successive surface elements in the x or w direction

being set to $\Delta x = \Delta w = 50$ nm. This level of discretization was sufficient to produce smooth profiles for the FF properties. To verify the convergence of these FF profiles, six points were selected for both $^{97}_{39}\text{Y}$ and $^{136}_{53}\text{I}$. Simulations were conducted in batches of 1000 ions. The simulations were terminated when the relative changes in probability, energy, and angle between two consecutive batches of simulations fell below 0.001 at each of the six selected points. The following (x, w) coordinates, measured in μm , were used for convergence: $(3, 0)$, $(5, 0)$, $(7, 0)$, $(4.5, 0.5)$, $(6.5, 0.5)$, and $(6, 1)$ for $^{97}_{39}\text{Y}$, and $(2, 0)$, $(3.5, 0)$, $(5, 0)$, $(3, 0.5)$, $(4.5, 0.5)$, and $(4, 1)$ for $^{136}_{53}\text{I}$. The $^{97}_{39}\text{Y}$ profiles converged after 30,000 simulations, whereas the $^{136}_{53}\text{I}$ profiles required 40,000 simulations to achieve convergence.

Figure 5 presents the results from the simulations and subsequent discretization. The incidence probability per unit area is displayed in Figures 5a and 5b. The probability profiles broaden as x increases, producing a plume-like pattern. Figures 5c and 5d illustrate the incidence ion energies. The circular pattern clearly demonstrates how the ions lose energy as they travel farther from the origin, with the energy loss as a function of distance being predominantly linear. Lastly, Figures 5e and 5f display the incidence angle of ions with respect to the x axis. As expected, ions closer to $w = 0$ have a low incidence angle, while ions farther away show higher incidence angles. In both the incidence energy and incidence angle plots, a few discrete FF paths are visible in the top-left region. These are highly unlikely occurrences, as is evident from the probability figures. The ion profiles also reveal the ranges of $^{97}_{39}\text{Y}$ and $^{136}_{53}\text{I}$ ions in U-10Mo to be approximately $8.5 \mu\text{m}$ and $6.5 \mu\text{m}$, respectively. The observed ranges, shown in Figure 5, are consistent with the data presented in Figure 1.

5.3 Fission fragment interactions with Xe gas bubbles

With the reference FF properties available, the next step involves simulating local FF–bubble interactions to quantify the gas bubble re-resolution rate. For these simulations, equilibrium Xe number densities were used for bubbles of all sizes. The equilibrium number densities were calculated using the van der Waals equation of state (EOS), as described in [42]:

$$n = \left(B + \frac{kT}{p} \right)^{-1} \quad (8)$$

$$n_{eq} = \left(B + \frac{kT}{p_{eq}} \right)^{-1} = \left(B + \frac{kTR_b}{2\gamma} \right)^{-1} \quad (9)$$

The equilibrium bubble pressure p_{eq} utilized in the EOS was derived from the Young-Laplace equation:

$$p_{eq} = \frac{2\gamma}{R_b} \quad (10)$$

where R_b is the bubble radius and $\gamma = 1.55 \text{ J/m}^2$ is the surface energy in U-10Mo [30]. The resulting equilibrium number densities are plotted as a function of bubble radius in Figure 6. Notably, the van der Waals EOS predicts a plateau in the equilibrium number density for smaller bubbles.

FF–bubble interactions should be simulated in a manner that accounts for all relevant recoils. To this end, five BCA simulations of $^{97}_{39}\text{Y}$ in U-10Mo were analyzed to evaluate recoil

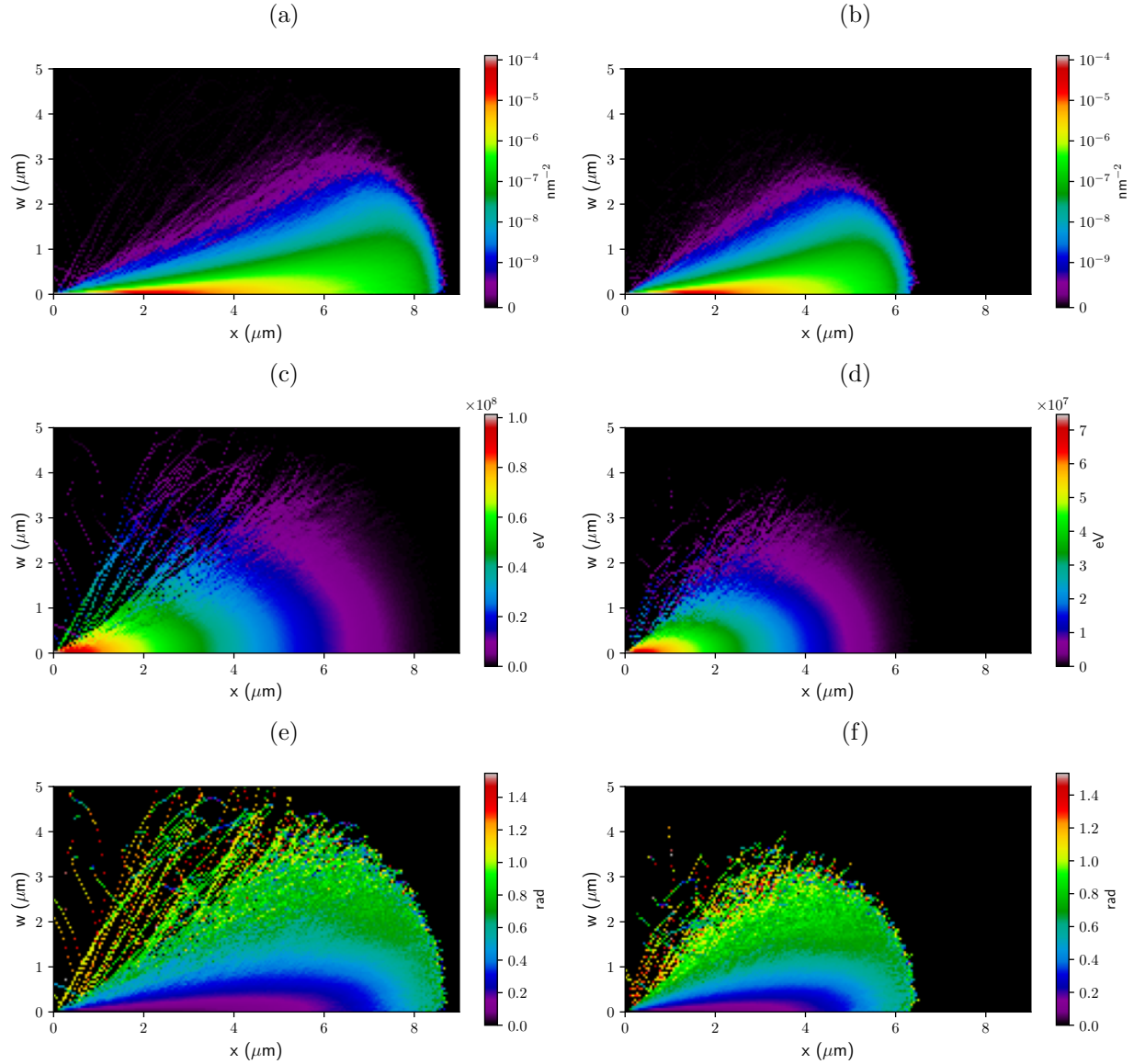


Figure 5: **Spatial distribution of FF incidence properties in U-10Mo.** Calculated FF properties in U-10Mo as a function of coordinates (x, w) for FFs initiated at the origin and directed along the x axis. Data represent the converged results from 30,000 simulations of $^{97}_{39}\text{Y}$ and 40,000 simulations of $^{136}_{53}\text{I}$. **a, b** Ion incidence probability per unit surface area centered at (x, w) for (a) $^{97}_{39}\text{Y}$ and (b) $^{136}_{53}\text{I}$. The probability profiles show a plume-like broadening as FFs travel further from the origin. **c, d** Average incidence energy for (c) $^{97}_{39}\text{Y}$ and (d) $^{136}_{53}\text{I}$, showing a predominantly linear energy loss with distance. **e, f** Average incidence angle relative to the x axis for (e) $^{97}_{39}\text{Y}$ and (f) $^{136}_{53}\text{I}$. Discrete paths visible in the low-probability regions of the energy and angle plots represent rare scattering events.

behavior. Figure 7 presents a scatter plot of the recoil displacement as a function of recoil energy. The maximum energy transferred to a recoil atom was about 1 MeV, with the recoil displacement being around 100 nm. While it is theoretically possible to transfer more than 1 MeV to a recoil in a head-on collision, such events are extremely rare. Therefore, it is

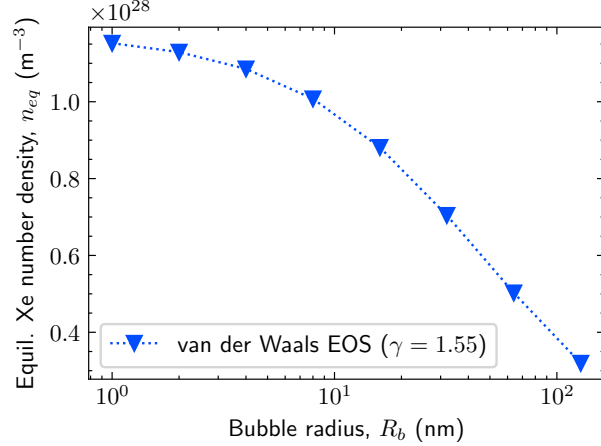


Figure 6: **Equilibrium Xe number density as a function of bubble radius.** The equilibrium Xe number density within the gas bubbles was calculated using the van der Waals EOS. The equilibrium bubble pressure used in the EOS was derived from the Young-Laplace equation, utilizing a surface energy of $\gamma = 1.55 \text{ J/m}^2$.

reasonable to assume that recoils generated by FFs more than $\delta = 100 \text{ nm}$ away from a gas bubble will not interact with that bubble. In the FF–bubble BCA simulations, the FFs were offset by a distance $D = R_b + \delta$ along the x axis from the bubble center. Recoil trajectories from one such simulation are visualized in Figure 8 using VisPy [43].

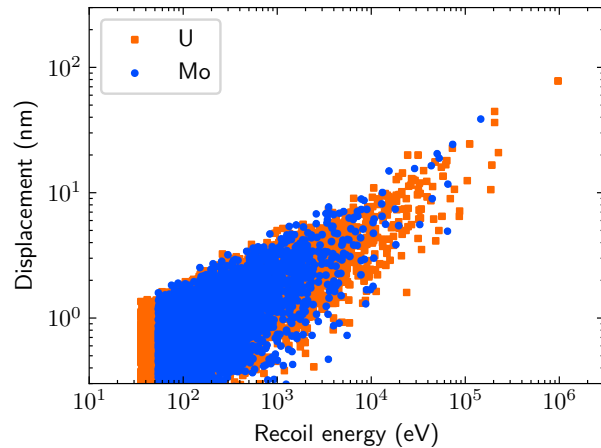


Figure 7: **Recoil displacement as a function of recoil energy in U-10Mo.** The scatter plot displays the data collected from five independent BCA simulations of $^{97}_{39}\text{Y}$ FFs. The maximum energy transferred to a recoil is approximately 1 MeV, resulting in a displacement of roughly 100 nm. This displacement ($\delta = 100 \text{ nm}$) was used to establish a spatial cut-off for subsequent simulations of FF–bubble interactions, assuming the recoils generated beyond this distance from a gas bubble surface are unlikely to interact with it.

Next, we determine which Xe recoils are re-solved. In this work, Xe atoms that end up at least $\lambda = 1 \text{ nm}$ away from the bubble surface are considered re-solved. In reality, the bubble surface is not a static structure due to the thermal fluctuations of the Xe atoms

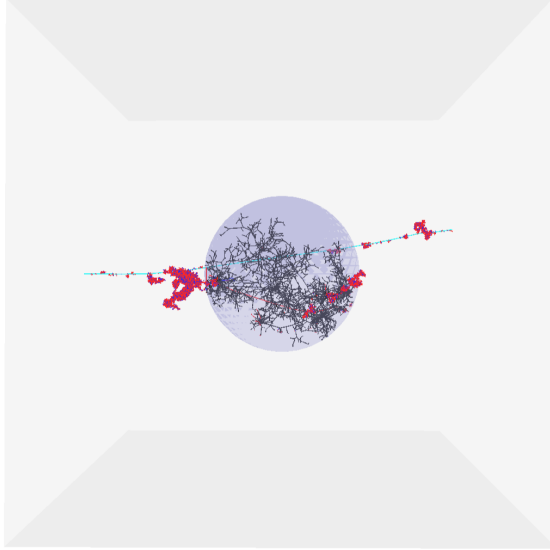


Figure 8: **Recoil trajectories from FF–bubble simulations.** Visualization of an individual BCA simulation where a 5 MeV $^{97}_{39}\text{Y}$ FF is incident on a Xe gas bubble with a 64 nm radius. Red, blue, black, and cyan lines represent U, Mo, Xe, and $^{97}_{39}\text{Y}$, respectively. In this specific interaction, 3,823 Xe recoils were generated, with 155 Xe atoms being displaced outside the bubble surface and 9 atoms being re-solved successfully (defined as being displaced ≥ 1 nm away from the bubble surface). The image was rendered using VisPy.

comprising it. As a result, a Xe atom that is just outside the surface is highly likely to return to the bubble within a short period. Thus, a finite annular region outside the bubble surface must be cleared by a Xe atom in order to be considered fully re-solved. Our choice of λ was informed by the existing literature on re-resolution simulations [10, 12, 9]. Figure 9 depicts the displacements of Xe recoils from an example simulation of a FF interacting with a bubble. From a plot of the recoil displacement as a function of recoil energy, such as Figure 9a, one can determine the minimum threshold energy E_{min} required for re-resolution, as λ and E_{min} are interconnected. While some re-resolution studies have subjectively chosen λ , others have focused on E_{min} as the criterion [15, 13]. Based on our simulations, we found E_{min} to be about 25 eV for $\lambda = 1$ nm. Additionally, Figure 9b shows that most Xe recoils originate close to the bubble surface and end up just outside it.

For FF–bubble simulations, both the FF energy E and off-center distance ℓ were discretized, with ℓ being defined as the minimum distance between the bubble center and the velocity vector of the FF at the beginning of the simulation. The energy discretization scheme depended on the specific FF being simulated, while ℓ discretization depended on the bubble radius. The ℓ values were selected to ensure adequate sampling of the region around the bubble radius R_b . A total of 5,000 BCA simulations were performed for each configuration. From these simulations, the number of re-solved Xe atoms was calculated. This number was then divided by the initial number of Xe atoms in the bubble in order to compute the re-solved bubble fraction χ . In other words, if a Xe gas bubble was at the origin $(x, w) = (0, 0)$, then $\chi(E', \ell')$ would be the re-solved bubble fraction due to the interaction of the bubble with a FF originating at $(x, w) = (-D, \ell')$ with an energy E' and moving

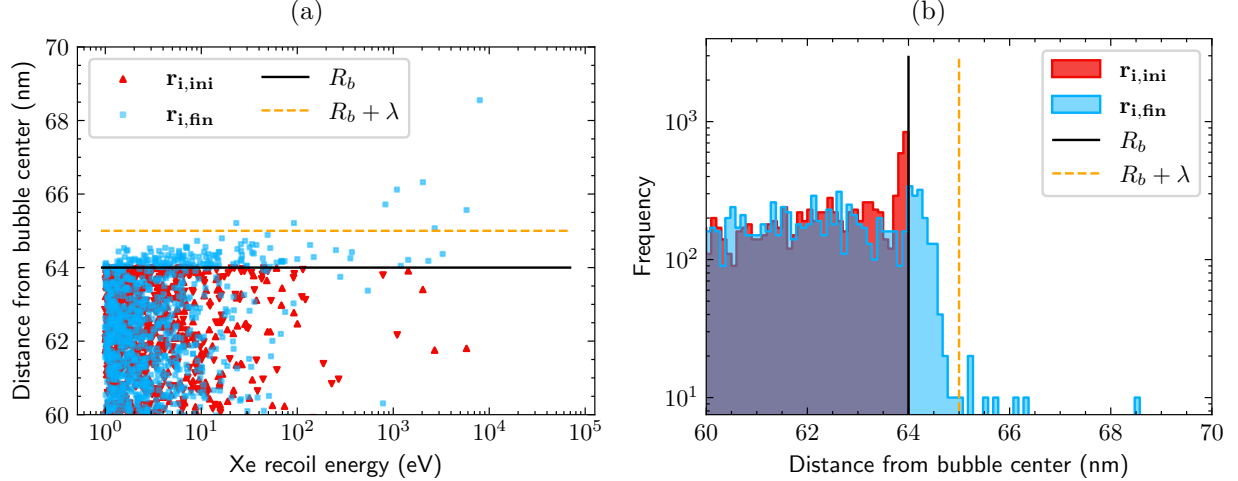


Figure 9: **Analysis of Xe recoils in a FF–bubble interaction.** The data were obtained from a simulation involving a 5 MeV ${}^{97}_{39}\text{Y}$ incident on a Xe bubble with a radius of $R_b = 64$ nm. **a** Initial ($\mathbf{r}_{i,\text{ini}}$) and final ($\mathbf{r}_{i,\text{fin}}$) positions of Xe recoils relative to the bubble center plotted as a function of recoil energy. The plot indicates a minimum threshold energy of $E_{\text{min}} \approx 25$ eV, corresponding to the re-resolution cut-off distance of $\lambda = 1$ nm. **b** Histogram showing the distribution of the initial and final positions of Xe recoils. The majority of the recoils originate near the bubble surface and are displaced to positions just outside the bubble surface. In both graphs, the distance from the bubble center is truncated to highlight the recoil behavior at the bubble–matrix interface.

along the x axis. The results for bubbles of two different sizes are shown in Figure 10. The 2 nm and 64 nm bubbles are representative of intragranular and intergranular bubbles, respectively. The error bars in the figure indicate 2σ deviations from the mean.

Using the simulation results and interpolation, it is now possible to estimate any reasonable $\chi(E', \ell')$ value. If \mathcal{I} is an interpolator that maps $X \rightarrow Y$, we can use the notation $y' = \mathcal{I}_X(x', X, Y)$ to indicate that the interpolator returns y' when x' is provided as input. Any arbitrary $\chi(E', \ell')$ can then be defined as follows:

$$\chi(E', \ell) = \mathcal{I}_{\mathcal{E}}(E', \mathcal{E}, [\chi(E, \ell)]_{E \in \mathcal{E}}) \quad (11)$$

$$\chi(E', \ell') = \mathcal{I}_{\mathcal{L}}(\ell', \mathcal{L}, [\chi(E', \ell)]_{\ell \in \mathcal{L}}) \quad (12)$$

where \mathcal{E} and \mathcal{L} are the sets of discrete energies and off-center distances used in the simulations, and E and ℓ are elements of those sets. In this work, $\mathcal{I}_{\mathcal{E}}$ is a PCHIP interpolator [44], and $\mathcal{I}_{\mathcal{L}}$ is a linear interpolator.

5.4 Calculation of ξ

Given that χ values are now known, we now proceed to calculate ξ . Consider a FF at the origin directed along the x axis and a bubble located at (x, w) . At this position, the FF has an average incidence angle $\alpha(x, w)$. Since the incidence angle changes minimally with variations in x and w , it is reasonable to assume the incidence angle in the vicinity of (x, w) is approximately $\alpha(x, w)$. Next, we identify a point (x', w') such that it is a distance D away from (x, w) and the line connecting these two points has a slope of $\tan(\alpha(x, w))$. A surface

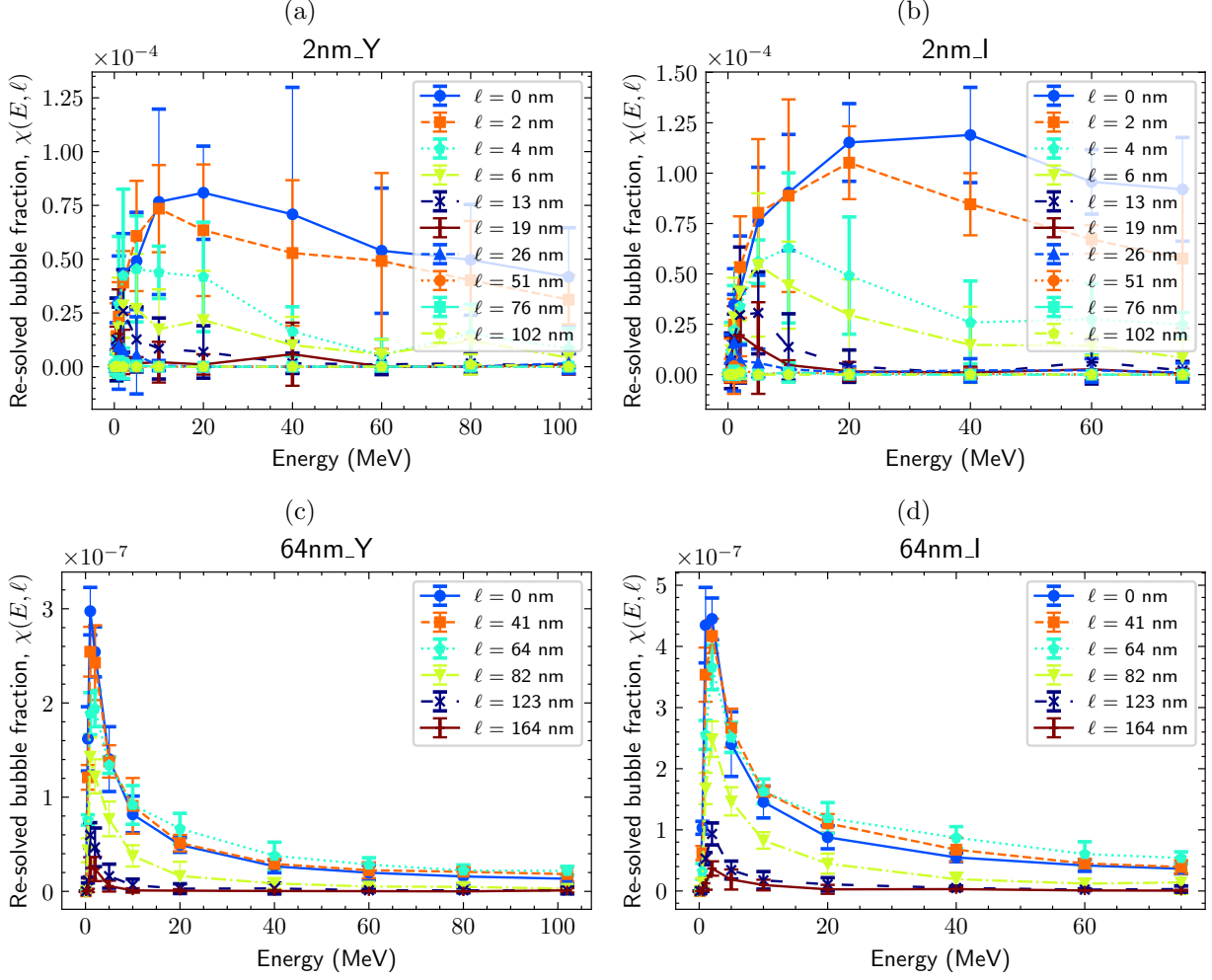


Figure 10: **Fraction of Xe atoms re-solved from gas bubbles (χ) as a function of FF energy (E) and off-center distance (ℓ).** The bubble is centered at the origin $(x, w) = (0, 0)$, and the FF is initiated at $(x, w) = -(R_b + \delta), \ell$ with an energy E and a direction along the x axis. R_b is the bubble radius and δ is the maximum recoil distance. **a, b** $\chi(E, \ell)$ for a bubble with a 2 nm radius interacting with incident **(a)** $^{97}_{39}\text{Y}$ and **(b)** $^{136}_{53}\text{I}$. **c, d** $\chi(E, \ell)$ for a bubble with a 64 nm radius interacting with incident **(c)** $^{97}_{39}\text{Y}$ and **(d)** $^{136}_{53}\text{I}$. Error bars represent 2σ deviations from the mean across 5,000 independent BCA simulations per configuration.

S perpendicular to this connecting line can then be constructed. The surface S is square in shape, with a side length of $2D = 2(R_b + \delta)$. This surface can then be meshed into small elements, as illustrated in Figure 11. The FF has specific probabilities of passing through each mesh element. If the FF traverses a mesh element m with a probability per unit area $p(r_m)$ and incidence energy $E(r_m)$, $\xi(x, w)$ can be calculated as:

$$\xi(x, w) = \sum_{m \in S} p(r_m) \frac{A_m}{\cos \alpha(x, w)} \chi(E(r_m), \|r_m - r_c\|) \quad (13)$$

where r_m denotes the coordinate of the center of the mesh element, and r_c denotes the center of the surface S . The probability of the FF passing through the mesh element m is

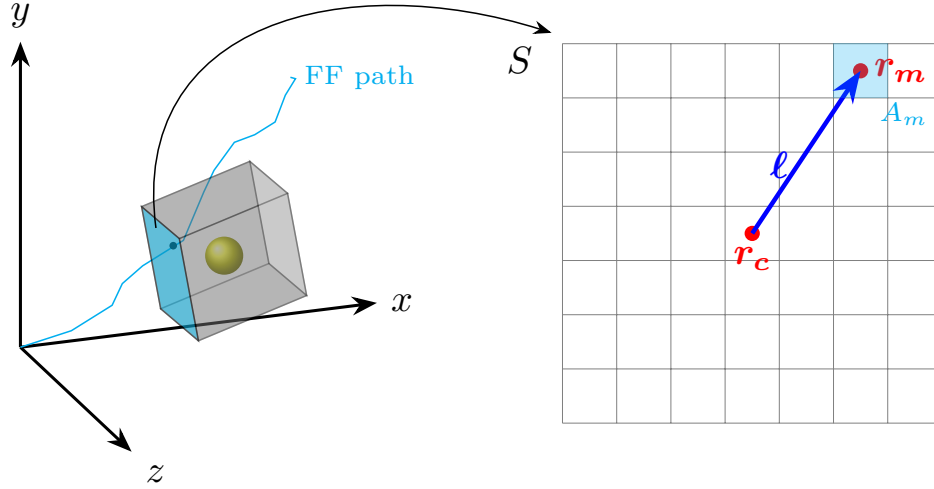


Figure 11: **Illustration of the ξ calculation scheme.** $\xi(x, w)$ denotes the re-solved bubble fraction for a bubble centered at (x, w) interacting with a FF originating at $(0, 0)$ with an initial velocity along the x axis. A square surface S with side length $2D$ is constructed at a distance $D = R_b + \delta$ distance from the bubble center, where the surface normal is oriented at an angle $\alpha(x, w)$ —the average FF incidence angle—relative to the x axis. The surface is discretized into small mesh elements. The FF may reach a mesh element m with a probability per unit area p_m and energy E , resulting in a re-solved fraction $\chi(E, \ell)$. Here, ℓ is the distance between the element center r_m and the surface center r_c . The total re-solved fraction ξ is obtained by summing the contributions from all possible trajectories through the mesh elements.

calculated as the product of $p(r_m)$ and the area of the mesh element A_m projected onto the plane perpendicular to the x axis. It is important to note that all FF trajectories that do not intersect S are ignored due to the extremely low probability of the FF or its associated recoils reaching the bubble.

Although the mesh elements shown in Figure 11 are of constant size, such a scheme is inefficient for the calculation of ξ . This inefficiency arises because R_b can be up to 50 times smaller than D . To address this, we implemented an adaptive meshing scheme. This scheme ensures a maximum mesh size of $R_b/2$ for $\ell \in [0, 2R_b]$, and 35 nm for $\ell \in (2R_b, D]$. The upper bounds of the mesh size were selected so that further refinement would not result in a relative change in ξ greater than 0.001.

ξ was calculated for all combinations of FF isotopes and bubble radii. The ξ_Y values for 2 nm and 64 nm bubbles are shown in Figures 12a and 12b, respectively. These ξ profiles can also be interpreted in a way that simplifies the calculation of the overall re-resolution rate b . If a bubble is located at the origin and a FF positioned at (x, w) is pointing in the $-x$ direction, the resulting ξ profiles would be exactly the same. Now, a discretized version of

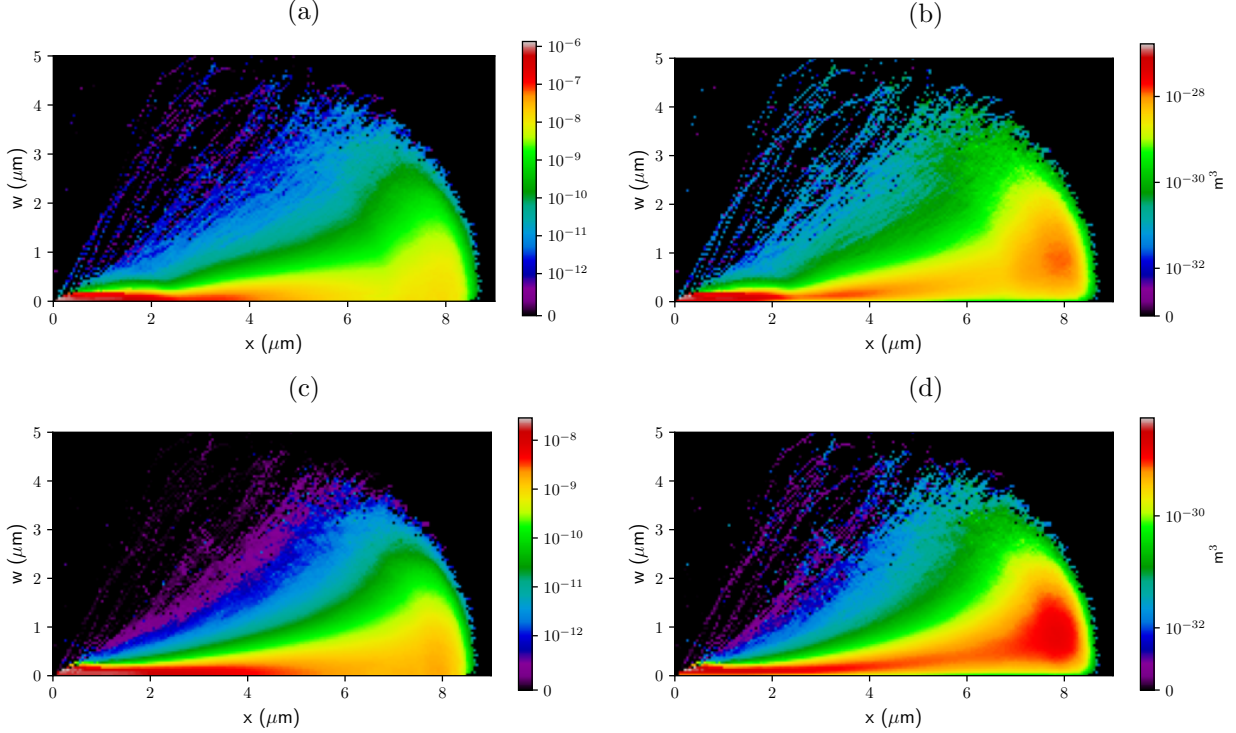


Figure 12: **Spatial distribution of ξ and $\xi\Delta V$ for ^{97}Y FFs.** The re-solved bubble fraction ξ and volume-weighted re-solved bubble fraction $\xi\Delta V$ are shown for a gas bubble centered at $(0, 0)$ and a ^{97}Y FF at (x, w) pointing toward the $-x$ direction. Note that this spatial arrangement is equivalent to the one in Figure 3 but represents the inverse of the setup shown in Figure 11. **a, b** ξ and $\xi\Delta V$ for a bubble radius of 2 nm. **c, d** ξ and $\xi\Delta V$ for a bubble radius of 64 nm.

Equation 5 can be formulated as:

$$b/\dot{F} = \sum_{k=Y,I} \sum \xi_k \Delta V \quad (14)$$

$$= \sum_{k=Y,I} \sum_{i,j \in V} \xi_k(x_{i,j}, w_{i,j}) [\pi(w_{i,j+1}^2 - w_{i,j}^2)(x_{i+1,j} - x_{i,j})] \quad (15)$$

where i, j denote the indices of the discrete grid points where ξ is evaluated. This is easy to calculate, because the ξ profiles have already been discretized. $\xi\Delta V$ profiles are also depicted in Figure 12 to show the significant effect of ΔV on re-resolution.

5.5 Homogeneous re-resolution rate

The total re-resolution rate of a given bubble can be determined by summing up all the values in $\xi_Y\Delta V$ profiles due to both ^{97}Y and ^{136}I . Figure 13 displays the re-resolution rates for bubbles with radii ranging from 1 nm to 128 nm. The error bars in the figure describe the uncertainty in b that arises solely from the uncertainty in χ . Since the ion profiles and ξ were computed using stringent convergence criteria, it is reasonable to assume that the majority of the uncertainty originates from χ . As a result, the error bars for b approximately correspond

to 2σ deviations. We also observe vanishingly small deviations for larger bubbles, simply because the probability of an interaction between a FF and larger bubbles is higher.

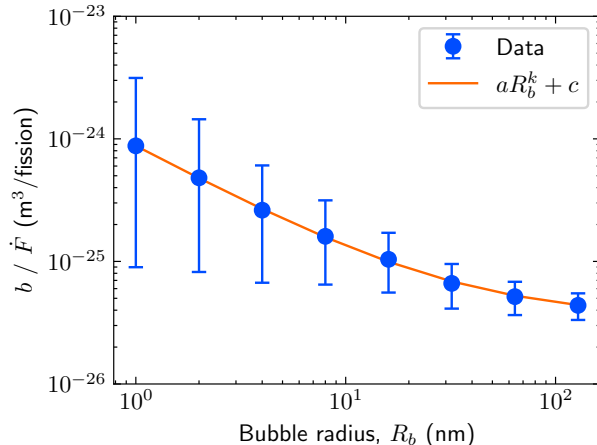


Figure 13: **Homogeneous re-resolution rate as a function of bubble radius R_b in U-10Mo.** The re-resolution rate was calculated at the equilibrium Xe number density n_{eq} for bubble radii ranging from 2 nm to 64 nm. The solid line represents a power-law fit of the form $aR_b^k + c$, which describes the data with high precision ($R^2 = 0.99986$). Error bars denote 2σ deviations from the mean, reflecting the uncertainty in χ .

While linear interpolations are sufficient to estimate re-resolution rates for arbitrary bubble radii, an approximate analytical function may be more suitable for use in higher-length-scale models. To this end, we propose the following functional form:

$$b/\dot{F} = aR_b^k + c \quad (16)$$

where $a = 8.43 \times 10^{-25}$, $k = -0.926$ and $c = 3.46 \times 10^{-26}$. R_b is in nm, and b/\dot{F} is in $\text{m}^3/\text{fission}$. The functional fit has a root mean squared error of $3.17 \times 10^{-27} \text{ m}^3/\text{fission}$ and a R^2 score of 0.99986.

5.6 Effect of bubble pressure

The effect of pressure on re-resolution was investigated by varying the Xe number density within bubbles of radii 8 nm and 64 nm. FF–bubble interaction simulations were conducted for $^{97}_{39}\text{Y}$ and $^{136}_{53}\text{I}$ ions with energies of 1 MeV and 20 MeV. The limited scope of simulations investigating the effect of bubble pressure is intended to show general trends in the re-resolution behavior of under- and over-pressurized bubbles. The resulting χ values that were calculated from these simulations are plotted in Figure 14, showing an inverse relationship between χ and n . The equation $\chi/\chi_{eq} = n_{eq}/n$, which was used to make the lines in Figure 14, fits the data with an R^2 score of 0.97. To understand the origin of this inverse relationship, further analysis of the simulation data was performed. It was found that the number of re-solved Xe atoms is almost an invariant with respect to the initial Xe number density in the bubble. Since χ is defined as the ratio of the number of re-solved Xe atoms to the total number of Xe atoms in the bubble, an inverse relation between χ and n naturally arises.

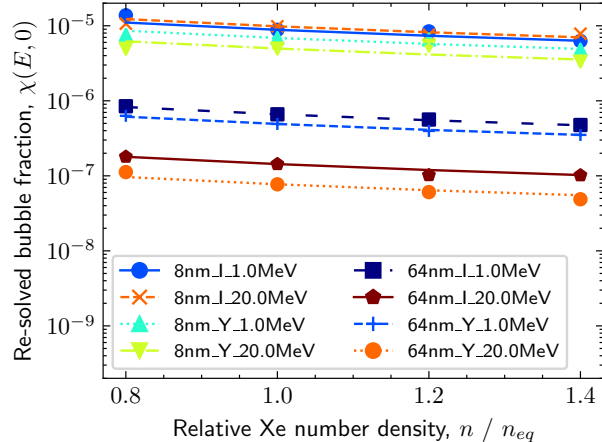


Figure 14: **Effect of Xe number density (n) on re-solved bubble fraction (χ)**. BCA simulations of FF interactions with under- and over-pressurized bubbles reveal an inverse relationship between χ and n . The lines represent the fit $\chi/\chi_{eq} = n_{eq}/n$, which accurately describes the data ($R^2 = 0.97$). This relationship arises because the number of re-solved Xe atoms remains nearly invariant regardless of the bubble's Xe number density. Data were obtained from 5,000 independent BCA simulations per configuration.

One possible explanation for the invariance of the number of re-solved atoms is that the re-resolution behavior is primarily affected by FF–bubble interactions close to the bubble surface, and the gas bubble surface area is independent of n .

Up to this point, the symbol b has been used to denote the re-resolution rate at the equilibrium Xe number density n_{eq} . Moving forward, b_{eq} will specifically refer to the re-resolution rate at equilibrium Xe density, while b will be reserved for the general re-resolution rate. The re-solved bubble fraction χ is related to ξ through Equation 13, and ξ is related to b through Equation 15. These relations can thus be used to relate the re-resolution rate directly to the Xe number density:

$$b \propto \xi \propto \chi \quad (17)$$

$$b/b_{eq} = n_{eq}/n \quad (18)$$

$$b = (aR_b^k + c) \left(\frac{n_{eq}}{n} \right) \dot{F} \quad (19)$$

where R_b is in nm, n is in m^{-3} , \dot{F} is in fission $\text{m}^{-3} \text{s}^{-1}$, and b is in s^{-1} . Equation 19 now describes the fission gas bubble re-resolution rate as a function of bubble size, bubble pressure, and fission rate.

6 Discussion

Figure 15 compares the re-resolution rate calculated in this work against the literature values for UO_2 , UC, and U-10Mo. Setyawan et al. performed MD simulations of gas bubbles in UO_2 , with the radii ranging from 0.6 nm to 3 nm [9]. The slope of $\ln b$ vs. $\ln R_b$ in UO_2 is similar to that observed in our work, albeit the re-resolution rate in UO_2 is nearly one order of

magnitude lower than in U-10Mo. Matthews et al. conducted BCA simulations to evaluate the re-resolution rate for a wide range of bubble radii in UC [13]. The slope of $\ln b$ vs. $\ln R_b$ in UC is flatter than in U-10Mo. Interestingly, an intersection between the two rates is also observed: the re-resolution rate is higher in U-10Mo for smaller bubbles, but higher in UC for larger bubbles. Despite these differences, the re-resolution rates in UO₂, UC, and U-10Mo (this work) are remarkably close, with the variation often being less than one order of magnitude. We could not compare our results against U-Zr because Mao et al. simulated all interactions at a fixed distance of 2 μm between the FFs and the bubbles [14]. Thus, their data do not directly lead to an overall re-resolution rate.

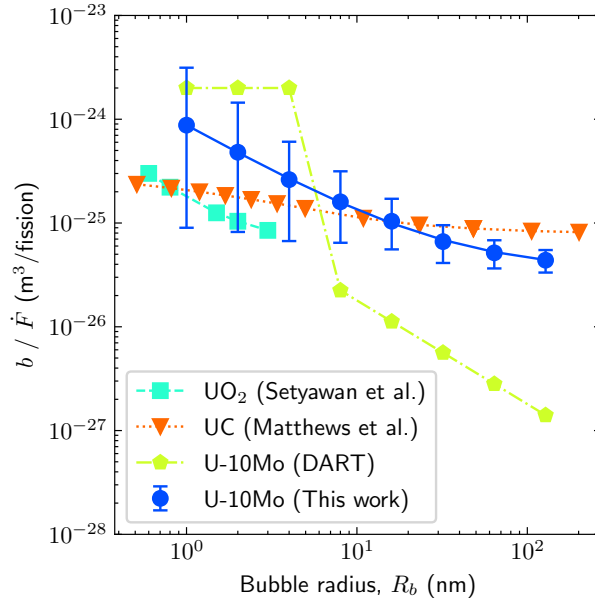


Figure 15: **Comparison of the re-resolution rates in UO₂, UC, and U-10Mo.** The re-resolution rates in various nuclear materials are shown as a function of bubble radius R_b . For UO₂, the re-resolution rate is dominated by the heterogeneous mechanism, which is driven by the thermal spikes resulting from the electronic stopping of FFs. In contrast, for UC and U-10Mo, re-resolution is primarily governed by the homogeneous mechanism (nuclear stopping) since their higher electronic conductivities suppress thermal spike formation. The piecewise re-resolution model for U-10Mo employed in the DART code is also included for comparison.

Finally, we compare the computed re-resolution rate from our work against the existing re-resolution model of U-10Mo as implemented in DART. The model is defined as follows:

$$b_{dart} = b_0 \cdot \dot{F} \cdot G \quad (20)$$

$$G = \begin{cases} 1 & , R_b \leq \lambda \\ 1 - \left(\frac{R_b - R_{resol}}{R_b}\right)^3 & , R_b > \lambda \end{cases} \quad (21)$$

where b_0 is the bubble destruction probability, and G is a piecewise function representing different re-resolution modes for small and large gas bubbles. In the piecewise function G , λ is the gas-atom knock-out distance and R_{resol} is the thickness of the annular region within which all gas-atoms are considered to be knocked out. The parameters b_0 , λ , and R_{resol}

are treated as adjustable, and were optimized to the following values: $b_0 = 2 \times 10^{-18} \text{ cm}^3$, $\lambda = 5 \times 10^{-7} \text{ cm}$, and $R_{resol} = 3 \times 10^{-9} \text{ cm}$. It is important to note that since the parameters λ and R_{resol} are not coupled, the re-resolution rate exhibits a discontinuity when the bubble radius is λ . According to Ye et al. [4], this is due to the strong trapping effects of grain boundaries on intergranular bubbles.

The re-resolution rate calculated in this work is slightly lower than the DART model prediction for intragranular bubbles but significantly higher for intergranular bubbles. In fact, the difference can be as large as two orders of magnitude for intergranular bubbles. This large discrepancy potentially arises from the mixing of trapping effects in the re-resolution rate in the DART model. However, the trapping effect of the grain boundaries is negligible in the time frame of collision cascades. It is therefore recommended that the re-resolution rate and trapping rate be implemented as separate processes in the higher-length-scale models of gas bubble evolution. This separation would provide greater flexibility for modeling the complex behavior of gas bubbles in the fuel under different contexts. For instance, the grain boundary diffusion coefficient of Xe in U-10Mo can be 15 orders of magnitude higher than the intrinsic diffusion coefficient at approximately 600 K [45]. In a gas bubble evolution model, the Xe trapping rate for intergranular bubbles could therefore be set 15 times higher than for intragranular bubbles, while the re-resolution rate could be independently specified using the analytical model developed in this work. By decoupling these two rates, the re-resolution rate would not be confounded with the trapping rate, enabling more accurate predictions of gas bubble behavior in U-10Mo.

7 Conclusions

This study combined BCA and MD simulations to provide a comprehensive, physics-based understanding of the Xe gas bubble re-resolution rate in U-10Mo nuclear fuel. Our findings reveal that homogeneous re-resolution driven by nuclear stopping is the only active mechanism in U-10Mo, as heterogeneous re-resolution via electron stopping is highly improbable. A systematic approach was employed, involving profiling FF behavior, evaluating the interactions between FFs and Xe gas bubbles, and integrating the results into a physical model. The computed re-resolution rate spanned from $4.4 \times 10^{-26} \dot{F} \text{ s}^{-1}$ for the largest intergranular bubble to $8.8 \times 10^{-25} \dot{F} \text{ s}^{-1}$ for the smallest intragranular bubble, with \dot{F} expressed in fission/m³/s. Furthermore, our simulations demonstrated an inverse relationship between the re-resolution rate and Xe number density, indicating that higher bubble pressures suppress re-resolution. These results provide critical insights into the fundamental mechanisms underpinning gas bubble behavior in nuclear fuels, and establish a robust foundation for higher-length-scale models of U-10Mo.

8 Data availability

All data described in this work can be found at <https://osf.io/eubd6/>.

9 Code availability

The RustBCA fork containing the implementation of SPHEREINCUBOID geometry is available at <https://github.com/ATM-Jahid/RustBCA>.

10 Acknowledgements

This work was supported by the U.S. Department of Energy, Office of Material Management and Minimization, National Nuclear Security Administration, under DOE-NE Idaho Operations Office Contract DE-AC07-05ID14517. This manuscript has been authored in part by Battelle Energy Alliance, LLC with the U.S. Department of Energy. The publisher, by accepting the article for publication, acknowledges that the U.S. Government retains a nonexclusive, paid-up, irrevocable, worldwide license to publish or reproduce the published form of this manuscript, or allow others to do so, for U.S. Government purposes. This research made use of the resources of the High Performance Computing Center at Idaho National Laboratory, which is supported by the Office of Nuclear Energy of the U.S. Department of Energy and the Nuclear Science User Facilities.

11 Author contributions

A.H. conceptualized the study, performed the simulations, and analyzed the data. A.H. also prepared the original draft of the manuscript. L.M. and M.S. contributed to the MD simulation design and assisted with the initial draft. B.B. provided supervision, project administration, and funding acquisition. B.B. also performed the final review and editing of the manuscript.

12 Competing interests

The authors declare no competing interests.

References

- [1] M.K. Meyer, J. Gan, J.F. Jue, D.D. Keiser, E. Perez, A. Robinson, D.M. Wachs, N. Woolstenhulme, G.L. Hofman, and Y.S. Kim. Irradiation performance of u-mo monolithic fuel. *Nuclear Engineering and Technology*, 46(2):169–182, 2014.
- [2] Benjamin Beeler, Yongfeng Zhang, and Yipeng Gao. An atomistic study of grain boundaries and surfaces in γ u-mo. *Journal of Nuclear Materials*, 507:248–257, 2018.
- [3] Benjamin W Beeler, James I Cole, Sourabh Bhagwan Kadambi, Linu Malakkal, Larry K Aagesen Jr, Gerard Hofman, ATM Jahid Hasan, Shenyang Hu, Curt Lavender, Sean Masengale, et al. Microstructural-level fuel performance modeling of u mo monolithic

- fuel. Technical Report INL/EXT-21-65319, Idaho National Lab.(INL), Idaho Falls, ID (United States), 2021.
- [4] Bei Ye, Aaron Oaks, Shenyang Hu, Benjamin Beeler, Jeff Rest, Zhi-Gang Mei, and Abdellatif Yacout. Integrated simulation of u-10mo monolithic fuel swelling behavior. *Journal of Nuclear Materials*, page 154542, 2023.
 - [5] DR Olander and D Wongsawaeng. Re-resolution of fission gas—a review: Part i. intragranular bubbles. *Journal of nuclear materials*, 354(1-3):94–109, 2006.
 - [6] David C Parfitt and Robin W Grimes. Predicted mechanisms for radiation enhanced helium resolution in uranium dioxide. *Journal of Nuclear Materials*, 381(3):216–222, 2008.
 - [7] RS Nelson. The stability of gas bubbles in an irradiation environment. *Journal of Nuclear Materials*, 31(2):153–161, 1969.
 - [8] JA Turnbull. The distribution of intragranular fission gas bubbles in uo2 during irradiation. *Journal of Nuclear Materials*, 38(2):203–212, 1971.
 - [9] Wahyu Setyawan, Michael WD Cooper, Kenneth J Roche, Richard J Kurtz, Blas P Uberuaga, David A Andersson, and Brian D Wirth. Atomistic model of xenon gas bubble re-resolution rate due to thermal spike in uranium oxide. *Journal of Applied Physics*, 124(7), 2018.
 - [10] Daniel Schwen, M Huang, P Bellon, and RS Averback. Molecular dynamics simulation of intragranular xe bubble re-resolution in uo2. *Journal of Nuclear Materials*, 392(1):35–39, 2009.
 - [11] M Huang, D Schwen, and Robert S Averback. Molecular dynamic simulation of fission fragment induced thermal spikes in uo2: Sputtering and bubble re-resolution. *Journal of nuclear materials*, 399(2-3):175–180, 2010.
 - [12] K Govers, CL Bishop, DC Parfitt, SE Lemehov, M Verwerft, and RW Grimes. Molecular dynamics study of xe bubble re-resolution in uo2. *Journal of Nuclear Materials*, 420(1-3):282–290, 2012.
 - [13] Christopher Matthews, Daniel Schwen, and Andrew C Klein. Radiation re-resolution of fission gas in non-oxide nuclear fuel. *Journal of Nuclear Materials*, 457:273–278, 2015.
 - [14] Wenlue Mao, Jinli Cao, Xinfu He, Yonggang Li, Qirong Zheng, Wen Yang, and Qi Luo. Monte carlo simulation of intragranular xe bubble re-resolution in uzr nuclear fuels. *Nuclear Instruments and Methods in Physics Research Section B: Beam Interactions with Materials and Atoms*, 560:165623, 2025.
 - [15] C Ronchi and PT Elton. Radiation re-resolution of fission gas in uranium dioxide and carbide. *Journal of Nuclear Materials*, 140(3):228–244, 1986.

- [16] Thomas Jarrin, Antoine Jay, Nicolas Richard, and Anne Hé meryck. Coping with the stochasticity of collision cascades in molecular dynamics simulations. *Nuclear Instruments and Methods in Physics Research Section B: Beam Interactions with Materials and Atoms*, 500:1–9, 2021.
- [17] Roger E Stoller. The influence of pka direction on displacement cascade evolution. *MRS Online Proceedings Library*, 650:351–356, 2000.
- [18] Z G Wang, C Dufour, E Paumier, and M Toulemonde. The se sensitivity of metals under swift-heavy-ion irradiation: a transient thermal process. *Journal of Physics: Condensed Matter*, 6(34):6733, aug 1994.
- [19] M. Toulemonde, W. Assmann, C. Trautmann, and F. Grüner. Jetlike component in sputtering of lif induced by swift heavy ions. *Phys. Rev. Lett.*, 88:057602, Jan 2002.
- [20] Paramita Patra, S. A. Khan, M. Bala, D. K. Avasthi, and S. K. Srivastava. Assessing a thermal spike model of swift heavy ion–matter interactions via pd1-xnix/si interface mixing. *Phys. Chem. Chem. Phys.*, 21:16634–16646, 2019.
- [21] DM Duffy and AM Rutherford. Including the effects of electronic stopping and electron–ion interactions in radiation damage simulations. *Journal of Physics: Condensed Matter*, 19(1):016207, 2006.
- [22] Yeon Soo Kim, G Hofman, J Rest, GV Shevlyakov, and SSCR RIAR. Characterization of intergranular fission gas bubbles in u-mo fuel. Technical report, Argonne National Laboratory (ANL), 2008.
- [23] Jon T Drobný and Davide Curreli. Rustbca: A high-performance binary-collision-approximation code for ion-material interactions. *Journal of Open Source Software*, 6(64):3298, 2021.
- [24] C Varelas and J Biersack. Reflection of energetic particles from atomic or ionic chains in single crystals. *Nuclear Instruments and Methods*, 79(2):213–218, 1970.
- [25] W Möller and W Eckstein. Tridyn—a trim simulation code including dynamic composition changes. *Nuclear Instruments and Methods in Physics Research Section B: Beam Interactions with Materials and Atoms*, 2(1-3):814–818, 1984.
- [26] Wolfgang Eckstein. *Computer simulation of ion-solid interactions*, volume 10. Springer Science & Business Media, 2013.
- [27] A. P. Thompson, H. M. Aktulga, R. Berger, D. S. Bolintineanu, W. M. Brown, P. S. Crozier, P. J. in 't Veld, A. Kohlmeyer, S. G. Moore, T. D. Nguyen, R. Shan, M. J. Stevens, J. Tranchida, C. Trott, and S. J. Plimpton. LAMMPS - a flexible simulation tool for particle-based materials modeling at the atomic, meso, and continuum scales. *Comp. Phys. Comm.*, 271:108171, 2022.

- [28] D E Smirnova, A Yu Kuksin, S V Starikov, V V Stegailov, Z Insepov, J Rest, and A M Yacout. A ternary eam interatomic potential for u-mo alloys with xenon. *Modelling and Simulation in Materials Science and Engineering*, 21(3):035011, mar 2013.
- [29] S.V. Starikov, L.N. Kolotova, A.Yu. Kuksin, D.E. Smirnova, and V.I. Tseplyaev. Atomistic simulation of cubic and tetragonal phases of u-mo alloy: Structure and thermodynamic properties. *Journal of Nuclear Materials*, 499:451–463, 2018.
- [30] B. Beeler and Y. Zhang. The reconciliation and validation of a combined interatomic potential for the description of xe in γ u-mo. *Frontiers in Nuclear Engineering, under review*, 2018.
- [31] G. E. Norman, S. V. Starikov, V. V. Stegailov, I. M. Saitov, and P. A. Zhilyaev. Atomistic modeling of warm dense matter in the two-temperature state. *Contrib. Plasma Phys.*, 53(2):129–139, 2013.
- [32] V. V. Pisarev and S. V. Starikov. Atomistic simulation of ion track formation in UO₂. *J. Phys. Condens. Matter*, 26(47):475401, 2014.
- [33] AM Rutherford and DM Duffy. The effect of electron-ion interactions on radiation damage simulations. *Journal of Physics: Condensed Matter*, 19(49):496201, 2007.
- [34] Zi Li, Cong Wang, Jize Zhao, Wei Kang, and Ping Zhang. Theoretical study on electron-phonon coupling factor and electron-ion nonequilibrium process in uranium. *Physics of Plasmas*, 24(2), 2017.
- [35] LN Kolotova and SV Starikov. Atomistic simulation of defect formation and structure transitions in u-mo alloys in swift heavy ion irradiation. *Journal of Nuclear Materials*, 495:111–117, 2017.
- [36] JK Chen, DY Tzou, and JE Beraun. A semiclassical two-temperature model for ultrafast laser heating. *International journal of heat and mass transfer*, 49(1-2):307–316, 2006.
- [37] Robert William Mills. *Fission product yield evaluation*. PhD thesis, University of Birmingham, 1995.
- [38] AM Phillips, GS Mickum, and DE Burkes. Thermophysical properties of u-10mo alloy. Technical report, Idaho National Laboratory (INL), 2010.
- [39] Benjamin Beeler, Shenyang Hu, Yongfeng Zhang, and Yipeng Gao. A improved equation of state for xe gas bubbles in γ u-mo fuels. *Journal of Nuclear Materials*, 530:151961, 2020.
- [40] Giovanni Bussi, Davide Donadio, and Michele Parrinello. Canonical sampling through velocity rescaling. *The Journal of chemical physics*, 126(1), 2007.
- [41] Alexander Stukowski. Visualization and analysis of atomistic simulation data with ovito—the open visualization tool. *Modelling and simulation in materials science and engineering*, 18(1):015012, 2009.

- [42] Donald R Olander. Fundamental aspects of nuclear reactor fuel elements: solutions to problems. Technical report, California Univ., Berkeley (USA). Dept. of Nuclear Engineering, 1975.
- [43] Luke Campagnola, Almar Klein, Eric Larson, Cyrille Rossant, and Nicolas P Rougier. Vispy: harnessing the gpu for fast, high-level visualization. In *Proceedings of the 14th Python in Science Conference*, 2015.
- [44] Frederick N Fritsch and Judy Butland. A method for constructing local monotone piecewise cubic interpolants. *SIAM journal on scientific and statistical computing*, 5(2):300–304, 1984.
- [45] ATM Jahid Hasan and Benjamin Beeler. Calculation of grain boundary diffusion coefficients in γ u-mo using atomistic simulations. *Journal of Nuclear Materials*, page 155190, 2024.